



**HAL**  
open science

## Understanding the surface chemistry of carbon nanotubes: Toward a rational design of Ru nanocatalysts

Bruno F Machado, Mustapha Oubenali, M. Rosa Axet, T. Trang nguyen, Meltem Tunckol, Maria Girleanu, Ovidiu Ersen, I.C. Gerber, Philippe Serp

### ► To cite this version:

Bruno F Machado, Mustapha Oubenali, M. Rosa Axet, T. Trang nguyen, Meltem Tunckol, et al.. Understanding the surface chemistry of carbon nanotubes: Toward a rational design of Ru nanocatalysts. Journal of Catalysis, 2014, 309, pp.185-198. 10.1016/j.jcat.2013.09.016 . hal-01969547

**HAL Id: hal-01969547**

**<https://hal.insa-toulouse.fr/hal-01969547>**

Submitted on 14 Jan 2019

**HAL** is a multi-disciplinary open access archive for the deposit and dissemination of scientific research documents, whether they are published or not. The documents may come from teaching and research institutions in France or abroad, or from public or private research centers.

L'archive ouverte pluridisciplinaire **HAL**, est destinée au dépôt et à la diffusion de documents scientifiques de niveau recherche, publiés ou non, émanant des établissements d'enseignement et de recherche français ou étrangers, des laboratoires publics ou privés.



## Understanding the surface chemistry of carbon nanotubes: Toward a rational design of Ru nanocatalysts



Bruno F. Machado<sup>a</sup>, Mustapha Oubenali<sup>a</sup>, M. Rosa Axet<sup>a</sup>, T. Trang NGuyen<sup>a</sup>, Meltem Tunckol<sup>a</sup>, Maria Girleanu<sup>b</sup>, Ovidiu Ersen<sup>b</sup>, Iann C. Gerber<sup>c,\*</sup>, Philippe Serp<sup>a,\*</sup>

<sup>a</sup> Laboratoire de Chimie de Coordination UPR CNRS 8241, composante ENSIACET, Université de Toulouse, UPS-INP-LCC, 4 allée Emile Monso, BP 44362, 31030 Toulouse Cedex 4, France

<sup>b</sup> Institut de Physique et Chimie des Matériaux de Strasbourg, UMR 7504 CNRS - Université de Strasbourg, 23 rue du Loess BP43, 67034 Strasbourg cedex 2, France

<sup>c</sup> Université de Toulouse, INSA, UPS, CNRS, LPCNO (IRSAMC), 135 avenue de Rangueil, F-31077 Toulouse, France

### ARTICLE INFO

#### Article history:

Received 28 July 2013

Revised 21 September 2013

Accepted 24 September 2013

Available online 26 October 2013

#### Keywords:

Supported catalyst

Nanoparticles

Carbon nanotubes

Ruthenium

Carbon support

Surface chemistry

### ABSTRACT

A comprehensive experimental and theoretical study of the surface chemistry of ruthenium nanoparticles supported on/in multi-walled carbon nanotubes (CNTs) is reported that could pave the way to the rational design of metal–carbon nanocomposites. It is shown that the oxidation of CNTs by nitric acid that creates various oxygen surface functional groups (SFGs) on the CNT external surface is a crucial step for metal grafting. In particular, it is demonstrated that carboxylic acid, carboxylic anhydride, and lactone groups act as anchoring centers for the Ru precursor, presumably as surface acetato ligands. The HNO<sub>3</sub> treatment that also allows CNT opening contributes to the endohedral Ru deposition. The stability of Ru nanoparticles, modeled by a Ru<sub>13</sub> cluster, on different adsorption sites follows the order: Gr-DV-(COOH)<sub>2</sub> > Gr-DV > Gr (where DV is a double vacancy and Gr the graphene surface). It is evidenced that, after a high-temperature treatment performed in order to remove the SFGs, the Ru/CNT material can react with oxygen from air via a surface reconstruction reaction, which reforms a stable Ru-acetato interface. The mechanism of this reaction has been investigated by DFT. These Ru/CNT catalysts are extremely stable, keeping a mean particle size <2 nm, even after heating at 973 K under a hydrogen atmosphere.

© 2013 Elsevier Inc. All rights reserved.

### 1. Introduction

Metal nanoparticles (NPs) exhibit size-dependent physical, chemical, and electrical properties that differ significantly from the bulk materials, due to the large fraction of surface atoms and the quantum confinement effect. The application of these nanostructures in areas such as heterogeneous catalysis, sensors, and microelectronics reflects their economic importance. Metal NPs deposited on a support are particularly suitable for catalysis applications. Carbon materials such as activated carbons, carbon blacks, and graphitic materials are widely used as support for metal NPs in fine chemistry catalysis and electrocatalysis [1], because of their high surface area, their stability and relative inertness, and potentially high electronic conductivity. Under the influence of the support, the properties of supported metal NPs are different from that of isolated NPs and strongly dependent not only on the particle size and surface composition, but also on the surface morphology and nature of metal–support interactions [2]. Understanding and developing catalysts with supported NPs requires comprehensive experimental and theoretical studies of their thermal, structural,

and dynamic properties [3]. The impact of (molecular) surface chemistry on all these properties should therefore be taken into consideration for the rational design of supported catalysts [4,5].

The relatively good knowledge of conventional oxide support (silica, alumina, zeolites) surface chemistry has already allowed the design, at the molecular level, of supported NPs and single-site catalysts [6]. For carbon materials, however, a complex surface chemistry often imposes the use of empiric approaches for catalyst preparation. The carbon surface contains heteroatoms (O, N, and H) in the form of surface functional groups (SFGs) by analogy to those appearing in organic compounds [7]. The presence of these groups can affect the preparation of carbon-supported catalysts, as they induce an acid–base and/or hydrophilic character to the carbon surface. Thus, even if it has been demonstrated since many years that oxygen SFGs play a crucial role in the wetting of carbon supports and can affect dispersion or sintering of the metal particles [8,9], it is still a matter of debate whether they also function as anchoring sites for NPs [10]. Fig. 1 shows the various oxygen-containing functionalities present on a carbonaceous surface, together with the products resulting from their thermal decomposition under an inert atmosphere [11]. It has been experimentally shown that the more acidic groups, such as the carboxylic ones, decrease the hydrophobic character of the carbon surface and positively

\* Corresponding authors.

E-mail address: [philippe.serp@ensiacet.fr](mailto:philippe.serp@ensiacet.fr) (P. Serp).

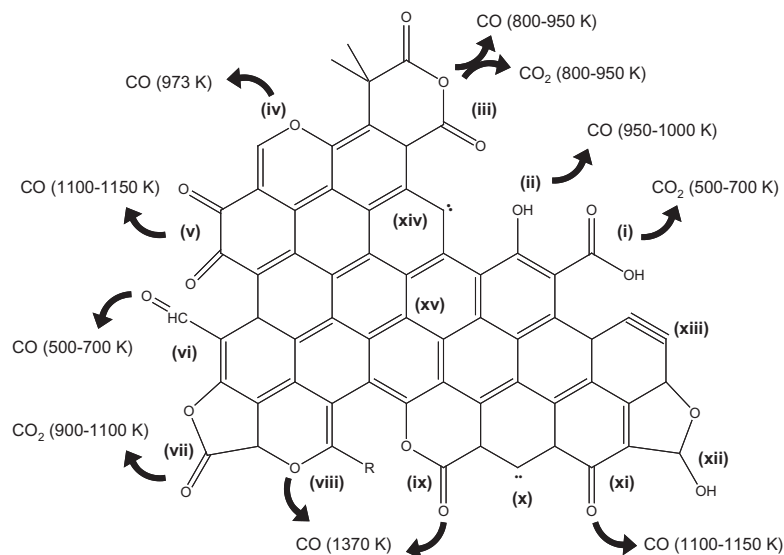


**Fig. 1.** Oxygen SFGs, and specific sites generally present on carbon surface: (i) carboxylic acid, (ii), phenol, (iii) carboxylic anhydride, (iv) ether, (v) quinone, (vi) aldehyde, (vii) lactone, (viii) chromene, (ix) pyrone, (x) carbene like species, (xi) carbonyl, (xii) lactol, (xiii) carbyne like species at armchair sites, (xiv) carbene like species at zigzag sites, and (xv) p electron density on carbon basal plane. The arrows show the decomposition product(s), from TPD deconvolution spectra (adapted from Ref. [11]).

impact the metal dispersion, providing anchoring sites for exchange of cationic metallic precursors [8,9]. On the other hand, the less acidic and thermally more stable SFGs, such as the carbonyls, favor the interaction between the metal particle and the carbon surface, thus minimizing sintering [8,9]. However, it is often omitted that the thermal stability of the carboxylic groups is limited to temperatures close to 673 K, and such temperatures are often used for the decomposition and/or reduction in the metallic phase.

Thus, the question concerning whether these oxygen SFGs affect the final metallic dispersion in a positive way due to their reactivity, or in a negative way (sintering of the metal NPs and loss of dispersion) as a consequence of their decomposition during catalyst pretreatments [12] remains open to discussion [13]. Moreover, in many cases, it is difficult to draw unequivocal conclusions, since the introduction or removal of oxygen SFGs can also lead to a difference in pore structure of the carbon support, in addition to the possibility of influencing the particle size. Indeed, micropores in the carbon support might be beneficial for metal dispersion. In that respect, the use of mesoporous carbon support, such as multi-walled carbon nanotubes (CNTs), the porosity of which being unchanged by heat treatment at  $T < 1273$  K, could allow a better control of catalyst preparation [14]. Furthermore, the possibility of specific interactions between the graphene surface defects and metal NPs and/or metallic precursors is an important subject in catalyst preparation. Finally, it has also been shown that the presence or absence of SFGs can also directly affect the catalytic behavior of the active phase [15–18]. We are particularly interested in carbon-supported ruthenium catalysts, the catalytic performances of which have already been evaluated in Fischer–Tropsch synthesis, ammonia synthesis/decomposition, hydrogenation, and liquid-phase oxidation reactions [1].

In this work, we report a detailed study on the nature of the ruthenium–carbon interface in Ru/CNT catalysts prepared from neutral Ru(0) organometallic precursors. Experimental data combined with density functional theory (DFT) calculations allowed to conclude that both Ru precursor and NPs are anchored on the external surface via the carboxylic surface groups, presumably via surface acetato ligands. Additionally, it is demonstrated that after a high-temperature treatment, performed to assist oxygen SFG removal, a surface reconstruction reaction occurs involving oxygen atoms present on the ruthenium NP surface and the carbon atoms remaining after oxygen SFG removal.

## 2. Experimental section

### 2.1. General methods

All reactions were carried out under argon atmosphere using standard Schlenk techniques or in an MBraun glove box. Solvents were purified by standard methods or by a MBraun SPS-800 solvent purification system. [Ru(COD)(COT)] was purchased from Nanomeps, Toulouse, 9-anthracenecarboxylic acid from Avocado, [Ru<sub>3</sub>(CO)<sub>12</sub>], 9-anthracenecarboxaldehyde, 9-anthracenol, and anthracene from Sigma–Aldrich.

### 2.2. Synthesis

#### 2.2.1. Carbon nanotubes and supported catalysts

The CNTs were produced by chemical vapor deposition of ethylene in the presence of hydrogen on iron catalysts supported on hydroxyapatite. The as-produced samples were purified by HCl washing during 12 h at room temperature, then filtered, washed with deionized water repeatedly until neutrality of the rinsing waters, and dried for 3 days in an oven at 393 K to produce CNT<sub>p</sub>. The CNT surface was then modified by a concentrated nitric acid solution under reflux for 4 h (CNT<sub>o</sub>). The nanotubes were again filtered, washed with distilled water, and dried in an oven for 3 days at 393 K.

The ruthenium catalysts were prepared by excess solvent impregnation on two kind of supports consisting of purified (CNT<sub>p</sub>) and HNO<sub>3</sub> oxidized (CNT<sub>o</sub>) CNTs, using two different Ru(0) precursors, [Ru(COD)(COT)], (1,5-cyclooctadiene)(1,3,5-cyclooctatriene)ruthenium (**Ru1**), and [Ru<sub>3</sub>(CO)<sub>12</sub>] (**Ru2**). Given the reactivity of **Ru1** precursor, the metal impregnation was carried out in a Schlenk tube under argon atmosphere with 1 g CNTs and 50 mL of pentane (stirred 2 days at 318 K, under reflux). As for **Ru2** precursor, the same suspension was agitated for 12 h in air at room temperature. The impregnated samples were filtered and washed thoroughly with the pentane and dried at 393 K in an oven overnight. The catalysts were subsequently reduced in flowing H<sub>2</sub>/Ar mixture (80:20 in volume) at 573 K for 2 h.

#### 2.2.2. [Ru(COD)(COT)] reactivity toward anthracene derivatives

In a typical experiment, to a 15 mM solution of [Ru(COD)(COT)] (3.4 mg, 0.011 mmol) in acetone-d<sub>6</sub> (0.7 mL), 2 equivalents of an

anthracene derivative were added. The solution was introduced into a screw cap NMR tube, and a NMR spectrum was recorded at room temperature. The solution was heated at 318 K for 17 h and a second NMR spectrum was recorded at room temperature (9-anthracenecarboxylic acid: 4.7 mg; 9-anthracenecarboxaldehyde: 4.4 mg; 9-anthracenol: 4.1 mg; and anthracene: 3.8 mg).

### 2.2.3. [Ru(9-anthracenecarboxylate)<sub>2</sub>(COD)]

Hundred milligram (0.32 mmol) of [Ru(COD)(COT)] was dissolved in 5 mL of dry acetone. An excess of 9-anthracenecarboxylic acid (170 mg, 0.76 mmol) was added at once to the yellow solution. After 15 min stirring at 318 K, the solution turned dark orange. A yellow precipitate appeared after heating overnight. The solvent was filtered and the yellow solid was cleaned twice with 3 mL of dry acetone and twice with 10 mL of dry pentane. Yield: 130 mg (63%). <sup>1</sup>H NMR (300 MHz, CDCl<sub>3</sub>): δ (ppm) = 8.64 (m, 4H, CH arene), 8.59 (s, 1H, CH arene), 8.03 (m, 4H, CH arene), 7.48 (m, 8H, CH arene), 5.29 (m, 2H, CH COD), 4.07 (m, 2H, CH COD), 2.63 (m, 4H, CH<sub>2</sub> COD), 2.52 (m, 2H, CH<sub>2</sub> COD), 2.31 (m, 2H, CH<sub>2</sub> COD). <sup>13</sup>C NMR (75.5 Hz, CDCl<sub>3</sub>): δ (ppm) = 188.8 (s, COO<sup>-</sup>), 131.4 (Cq arene), 130.7 (CH arene), 130.0 (Cq arene), 129.1 (Cq arene), 128.9 (CH arene), 127.8 (CH arene), 125.9 (CH arene), 125.8 (CH arene), 90.7 (CH COD), 85.1 (CH COD), 32.1 (CH<sub>2</sub> COD), 27.8 (CH<sub>2</sub> COD). IR (neat) ν = 1488, 1471, 1444, 1429, 1395, 1314, 873, 782, 726 cm<sup>-1</sup>. Anal. calcd. (%) for C<sub>38</sub>H<sub>30</sub>O<sub>4</sub>Ru (651, 71 g/mol): C, 70.03; H, 4.64; found: C 69.81, H 4.66.

### 2.3. Characterization

<sup>1</sup>H and <sup>13</sup>C spectra were recorded on a Bruker Avance 400 MHz or Bruker Avance 300 MHz spectrometer. Chemical shifts are relative to SiMe<sub>4</sub> (<sup>1</sup>H and <sup>13</sup>C) using chemical shifts of the solvent as a secondary standard. Crystallographic data were collected at 180(2) K on an Agilent Technologies GEMINI EOS diffractometer using a monochromatic Mo Kα radiation (λ = 0.71073 Å) and equipped with an Oxford Cryosystems cooler device. The structure was solved by direct methods (SIR92) [19] and refined using the least-squares method on F<sup>2</sup> (SHELXL-97) [20]. All non-H atoms were refined with anisotropic displacement parameters. The hydrogen atoms were refined isotropically at calculated positions using a riding model with their Uiso values constrained to 1.5 Ueq of their pivot atoms for terminal sp<sup>3</sup> carbon atoms and 1.2 times for all other carbon atoms. Crystal data and refinement parameters are given in Table SI.11–12.

TEM images of the samples were taken on a JEOL 1011 transmission electron microscope. High-resolution images were obtained on a JEOL JEM 2100F transmission electron microscope with a field emission gun (TEM-FEG). Average diameters were calculated from statistical distributions of Ru nanoparticles on the TEM images. The experimental TEM data for the conventional analysis and electron tomography were acquired on a JEOL 2100F transmission electron microscope with a field emission gun operating at 200 kV, equipped by a probe corrector and a GATAN Tri-diem energy filter. Before observation, the powder was dispersed in ethanol by sonication, and several droplets were deposited onto a copper grid covered by a carbon holey membrane. For the tomographic analysis [21,22], the acquisition of the tilt series was performed using a high tilt sample holder by considering angles ranging from +70° to -70° and a tilt increment of 1.5°. The TEM images were acquired on a CCD detector (2048 × 2048 pixels) with a pixel size of 0.066 nm. The images of the tilt series were initially aligned using a cross-correlation algorithm. A refinement of this initial alignment was obtained by considering the centers of several Ru nanoparticles as fiducial markers. The volume reconstructions have been computed using iterative algorithms based on algebraic reconstruction techniques implemented in the TOMOJ

software, by considering 20 iterations. Visualization and quantitative analysis of the final volumes have been done by using the ImageJ software.

The X-ray diffraction (XRD) patterns were obtained using a Panalytical MPDPro powder diffractometer with Cu Kα radiation (λ = 0.15406 nm), equipped with a fast linear detector.

Micro-Raman spectra were taken on powder samples on a Perkin-Elmer 400F Raman spectrometer with 785 nm red laser irradiation.

Textural characterization of the materials was based on the nitrogen adsorption-desorption isotherms, determined at 77 K with a Quantachrome NOVA 4200e multi-station apparatus. The specific surface area (S<sub>BET</sub>) was calculated by multipoint BET analysis of the isotherm in the relative pressure range from 0.05 to 0.3. TPR/TPD spectra were obtained with a fully automated AMI-200 Catalyst Characterization Instrument (Altamira Instruments), equipped with a thermal conductivity detector (TCD) and a quadrupole mass spectrometer (Dymaxion 200 amu, Ametek). For TPR experiments, the sample was placed in a U-shaped quartz tube located inside an electrical furnace and heated at 5 K/min to 973 K under a 5 vol.% H<sub>2</sub> flow diluted with He (total flow rate of 30 cm<sup>3</sup>/min, STP); for TPD, the sample was heated to 1373 K using a constant flow rate of helium (25 cm<sup>3</sup>/min, STP). The H<sub>2</sub> consumption was followed by both TCD and mass spectrometry. The amounts of CO and CO<sub>2</sub> released during the thermal analysis were calibrated at the end of each analysis. This allowed the identification and quantification of the different types of oxygen SFG at the materials surface by analysis of the corresponding TPD spectra using the peak assignment and deconvolution procedures described by Figueiredo et al. [11].

The determination of the point of zero charge (pH<sub>PZC</sub>) of the samples was carried out according to the following procedure: 50 mL of a NaCl solution (0.01 M) was placed in a closed Erlenmeyer flask; the pH was then adjusted to a value between 2 and 12 using HCl (0.1 M) or NaOH (0.1 M) before the addition of 0.05 g of sample. The final pH was measured after 72 h continuous stirring at room temperature. The intersection point between the curve consisting of initial and final pH values with a 45° straight line yielded the pH<sub>PZC</sub> of the sample.

### 2.4. Computational details

DFT calculations were carried out using the Vienna *ab initio* simulation package VASP [23–26]. The code uses the full-potential projector augmented wave (PAW) framework [27,28]. Exchange-correlation effects have been approximated using the PBE functional [29] and applied in spin-polarized calculations. In order to model the interaction between the nanotubes' sidewalls and the grafted Ru nanoparticles, we have used a (7 × 7) primitive cell of graphene, presenting (or not) a di-vacancy of 555-777 type [30] and functionalized (or not) by carboxylic groups, and a nanocluster of Ru consisting of 13 atoms. This model, despite its rather small size, has been already able to provide interesting information on the interaction between transition metals nanoclusters and carbonaceous substrates. For instance, it has been used to investigate the enhancement of the catalytic performance of Ru nanoparticles due to the presence of a graphenic substrate [31] or in the studies of Pt nanoclusters binding to point defect in graphene [32], to understand CO-poisoning Pt nanoparticles adsorbed on graphene [33], and to propose theoretical insights into the oxygen reduction reaction on Pt nanoparticles grafted to graphene [34].

A kinetic-energy cutoff of 400 eV was found to be sufficient to achieve a total energy convergence within several meV considering a *k*-point sampling with a (3 × 3 × 1) grid. During geometry optimization runs, all the atoms were fully relaxed until forces on individual atoms were smaller than 0.02 eV/Å. Considering the

smearing issue, a Gaussian smearing with a width of 0.2 eV was used, while the tetrahedron method with Blöchl corrections [35] was used for accurate energy calculations. Diffusion barriers were estimated by the climbing image nudge elastic band (CI-NEB) method [36,37], with a force tolerance of 0.02 eV/Å and five intermediate geometries for the transition state search. An important parameter that describes the interaction between Ru<sub>13</sub> and the graphene layer is the adsorption energy defined as follows:

$$E_{ads} = E_{Ru_{13}@Graph} - E_{Ru_{13}} - E_{Graph},$$

where  $E_{Ru_{13}@Graph}$  stands for the total energy of the composite system, while  $E_{Ru_{13}}$  is the total energy of the ideal icosahedral structure, or the energy of the oxidized aggregate and  $E_{Graph}$  is the total energy of the graphene layer substrate, be it pristine or presenting a di-vacancy, be it decorated by carboxylic groups or not. Geometries were produced thanks to the 3D visualization program VESTA [38].

### 3. Results and discussion

#### 3.1. Supported ruthenium catalyst characterization

##### 3.1.1. CNT support characterization

The ruthenium catalysts were prepared by excess solvent impregnation on two kind of supports consisting of purified CNTs (**CNT<sub>p</sub>**) and HNO<sub>3</sub> oxidized (**CNT<sub>o</sub>**) CNTs, from two Ru(0) organometallic precursors, [Ru(COD)(COT)], (1,5-cyclooctadiene)(1,3,5-cyclooctatriene)ruthenium (**Ru1**), and [Ru<sub>3</sub>(CO)<sub>12</sub>] (**Ru2**). The detailed characterization of **CNT<sub>o</sub>** and **CNT<sub>p</sub>** as well as the mechanism of CNT nitric acid oxidation has been reported elsewhere [39]. Briefly, this reaction involves the initial rapid formation of carbonyl groups, which are consecutively transformed into phenol and carboxylic groups. The textural and chemical properties of the original and oxidized CNTs are reported in Table 1.

The main effects of HNO<sub>3</sub> oxidation are as follows: (i) a slight increase in the Raman  $I_D/I_G$  ratio, usually attributed to the presence of disordered carbon in CNT samples, the quantity of which decreases upon oxidation, (ii) an increase in the BET surface area and pore volume due to CNT tip opening, and (iii) the introduction of acidic carboxylic SFGs (among others), as shown by the appearance of a  $\nu_{C=O}$  band in IR, the change in PZC values, and the value of the TPD CO/CO<sub>2</sub> ratio (Table 1). Fitting of the TPD profiles (see SI.1) allows quantifying the amount of surface oxygenated species [40]. For **CNT<sub>p</sub>**, oxygen SFGs consist in 96  $\mu\text{mol/g}$  of lactone, 280  $\mu\text{mol/g}$  of anhydride, 520  $\mu\text{mol/g}$  of carboxylic acid, 590  $\mu\text{mol/g}$  of phenol, and 300  $\mu\text{mol/g}$  of carbonyl/quinone. For **CNT<sub>o</sub>**, a significant increase for each kind of groups was measured: 161  $\mu\text{mol/g}$  of lactone, 365  $\mu\text{mol/g}$  of anhydride, 840  $\mu\text{mol/g}$  of carboxylic acid, 1080  $\mu\text{mol/g}$  of phenol, and 840  $\mu\text{mol/g}$  of carbonyl/quinone. As far as the exo- or endohedral chemical functionalization is concerned, the quantification of oxygen SFGs present on the inner or outer surface is a difficult task. The CNT convex (outer) surface should be chemically more reactive because the convex arrangement of pyramidalized sp<sup>2</sup> carbon atoms is advantageously disposed for the formation of chemical bonds with reagent species. The concave (inner) surface should be more inert. However, the difference of reactivity between the inner and outer surfaces should decrease as CNT diameter increases. In order to distinguish

between exo- or endohedral chemical functionalization, a simple strategy was followed. **CNT<sub>o</sub>** were functionalized with a commercial glycidyl terminated epoxy resin with a  $M_n$  value of 355 (Scheme 1). A low molecular weight resin was preferred in order to favor high grafting density and to optimize diffusion for permitting the endohedral functionalization. The grafting of the phenoxy onto the CNT surface was achieved through blending the **CNT<sub>o</sub>** and the resin at 353 K. As mild heating was used, tributylamine (NBu<sub>3</sub>) was added to the reaction mixture as activator base. FTIR analysis was performed to verify the successful grafting. The spectrum of the epoxy grafted CNTs resembles to that of the neat epoxy, but with the presence of a carbonyl band at around 1717 cm<sup>-1</sup>. In order to visualize the polymeric chains on the CNT surface, the sample was treated with a TEM staining agent (RuO<sub>4</sub>). Fig. 2 shows a HREM micrograph and a typical longitudinal slice through the reconstructed volume obtained by TEM tomography of the epoxy grafted CNTs.

This image clearly shows that the grafted oligomers (<1.5 nm) have been homogeneously distributed on the external surface of the CNTs. To the best of our knowledge, this is the first evidence reported up to now of the absence of endohedral functionalization during the nitric acid oxidation of multi-walled CNTs. It is proposed that the absence of endohedral functionalization after HNO<sub>3</sub> treatment, which is capable of opening CNT tips, can be explained by the perfect inner surface of CNTs, which is less reactive than the defective outer surface. Indeed, we have previously shown that the formation of surface –COOH groups is barrierless on vacancies, while a perfect graphene layer is much less reactive [39].

Other CNT characteristics such as their purity (92%), mean external/internal diameter (18/6 nm), and  $d_{002}$  value (0.339 nm) were not affected by the HNO<sub>3</sub> treatment. TEM micrographs of **CNT<sub>p</sub>** and **CNT<sub>o</sub>** are provided in SI.2.

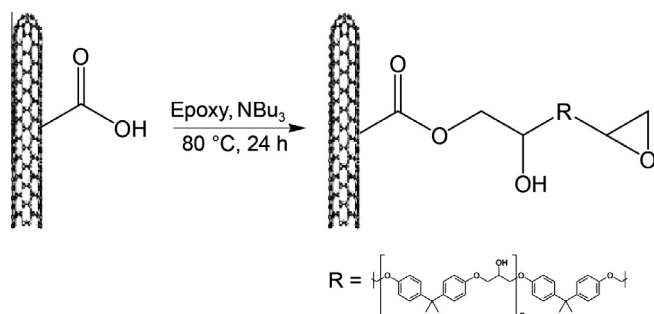
##### 3.1.2. Ru/CNT characterization

A series of 3 wt.% Ru/CNT catalysts have been prepared on **CNT<sub>p</sub>** and **CNT<sub>o</sub>** from the two organometallic precursors **Ru1** and **Ru2**. The Ru/CNT<sub>o</sub> samples have been further heat-treated under argon at 973 or 1173 K in order to evaluate the influence of oxygen SFG removal on metal particle size and surface chemistry. Several studies have shown that such a heat treatment can significantly change the activity and selectivity of CNT supported catalysts [15,18,41,42]. This modification of the support can affect the catalyst activity/selectivity either: (i) by direct modification of the support-NP interface (metal-support interaction), by inducing modification of particle size (sintering) or of the electronic transfer; or: (ii) by a modification of the microenvironment around the metal particle (hydrophilic/hydrophobic) that can modify the adsorption/desorption steps during catalysis. The characterization data of the series of catalysts is given in Table 2.

**3.1.2.1. Metal loading and Ru nanoparticle size and location.** The excess solvent impregnation method leads to different Ru loadings depending on the precursor used, higher loading being obtained when starting from the **Ru2** cluster. Since three ruthenium atoms are incorporated during the grafting process for each molecule of **Ru2**, compared to one for **Ru1**, the nuclearity of the precursor is

**Table 1**  
Textural and chemical characterization of the purified and functionalized supports.

Sample	Raman ( $I_D/I_G$ )	IR (cm <sup>-1</sup> )		BET (m <sup>2</sup> /g)	Pore vol. (cm <sup>3</sup> /g)	PZC	TPD ( $\mu\text{mol/g}$ )		
		$\nu_{C=C}$	$\nu_{C=O}$				CO	CO <sub>2</sub>	CO/CO <sub>2</sub>
CNT <sub>p</sub>	1.5	1570	–	134	0.302	7.6	1330	908	1.5
CNT <sub>o</sub>	1.6	1572	1724	172	0.344	3.5	2315	1365	1.7



**Scheme 1.** Illustration of the epoxy grafting to the CNT surface.

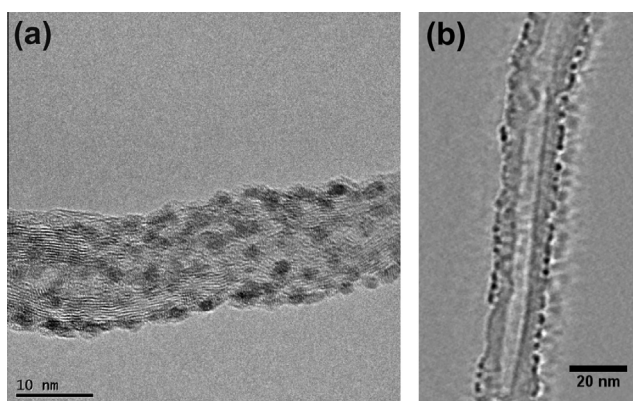


**Fig. 2.** (a) HRTEM micrograph, and (b) typical longitudinal slice through the reconstructed volume obtained by electron tomography for the chosen fragment of one of the epoxy grafted CNTs.

thought to be the main parameter that influences the metal loading. The different loadings cannot be explained by the reactivity of the precursor toward the surface since **Ru1** is more reactive than **Ru2** toward oxygen SFGs (as it will be discussed in Section 3.2). Higher loadings were also obtained on **CNTo** compare to **CNTp**, suggesting the implication of oxygen SFGs in the grafting process.

XRD patterns of the reduced Ru-based samples (reduction temperature 573 K) show peaks at  $2\theta \approx 26^\circ$  that corresponds to the (002) plane of CNTs, and reflections at  $38.7^\circ$ ,  $42.5^\circ$ ,  $44.2^\circ$ ,  $58.6^\circ$ , and  $69.8^\circ$  corresponding, respectively, to the (100), (002), (101), (102), and (110) planes of metallic ruthenium, which are consistent with an exclusive hexagonal geometry and establish the presence of Ru<sup>0</sup>. TPR data confirmed that a temperature of 573 K is sufficient to reduce the metal phase. The **Ru1** samples show diffraction peaks of lower intensity than the **Ru2** ones. For the Ru1/CNTp sample, the diffraction peaks were not visible due to the very low metal loading as well as to the very small size of NPs. The Ru

crystallite sizes were calculated from the widths of XRD peaks using the Scherrer equation. The Ru crystallite diameter was smaller when starting from the **Ru1** than with the **Ru2** precursor. This could be explained by a higher reactivity of **Ru1** during the grafting procedure (faster nucleation rate) and/or by the fact that we used two precursors of different nuclearity. The smaller particle size obtained from **Ru1** was confirmed by TEM observation (Fig. 3, and SI.3). XRD data and TEM analyses show that Ru crystallite mean diameter increased upon heat treatment. An overestimation of mean particle size measured by XRD was noticed, particularly for the **Ru2** samples where a stronger contribution of larger particles (6–8 nm) gives rise to the observed pattern. This increase is particularly sensitive after 973 K. We noticed that the endohedral Ru grafting was significantly higher on **CNTo** (opened tip CNTs, Fig. 3c) than on **CNTp**, whatever the precursor used. As previously shown, no endohedral functionalization occurs during the HNO<sub>3</sub> treatment, indicating a relatively good stability of small Ru NPs on the pristine surface. This was confirmed by DFT calculations, as shown in Section 3.2. We also investigated the influence of Ru NP location on their size and thermal stability. For **Ru1**, we found that the ruthenium nanoparticles located inside (NP<sub>in</sub>) **CNTo** are significantly smaller than the NP<sub>out</sub>. The mean NP<sub>in</sub> size is 1.1 nm, whereas the mean NP<sub>out</sub> size is 1.5 nm. This is an important issue that should be considered in confinement effect studies, when comparing the reactivity of metal catalysts. As far as the thermal stability is concerned, the NP<sub>in</sub> are more sensitive to sintering than the NP<sub>out</sub>, indicating a difference in stability of the adsorption sites or in NP diffusion. However, and even for Ru1/CNTo1173 sample, the mean NP<sub>in</sub> size remains smaller than the mean NP<sub>out</sub> size, due to template effect of CNT cavity preventing sintering.

**3.1.2.2. Study of the Ru–C interface by TPD analyses.** The TPD-MS profiles of the supported catalysts provide valuable information on the influence of oxygen SFGs on ruthenium grafting. The data obtained for the **Ru1** and **Ru2** series are presented in Fig. 4 and Table 2. Two main phenomena are observed: (i) the CO<sub>2</sub> evolution profile is much more affected by ruthenium deposition than the CO one, and (ii) the high-temperature treatment (Ru/CNTo1173 sample) contributes to a significant decrease in the oxygen SFG-releasing CO upon decomposition, except for the epoxy groups (peak at 870–880 K) (Fig. 4b and 4d).

As far as CO<sub>2</sub> evolution is concerned (Fig. 4a and 4c), ruthenium deposition on the **CNTo** surface leads to the disappearance of most of the carboxylic acid (peak at 565 K), anhydride (peak at 735 K), and lactone groups (peak at 950 K). Ruthenium deposition induces the formation of new CO<sub>2</sub> releasing groups at 640 and 742 K for **Ru1** and **Ru2**, respectively. The fact that (i) two very narrow peaks, characteristic of a catalytic decomposition, are observed in the CO<sub>2</sub> evolution profile for Ru1/CNTo and Ru2/CNTo and (ii) that their position depends on the nature of the ruthenium precursor (different

**Table 2**  
Physical and textural characterization data of the Ru catalysts.

Sample	Ru loading (%)	BET (m <sup>2</sup> /g)	Ru NP (nm) <sup>a</sup>	Ru NP (nm) <sup>b</sup>	NP <sub>out</sub> /NP <sub>in</sub>	TPR (K)	TPD (μmol/g)	
							CO	CO <sub>2</sub>
Ru1/CNTp	0.3	n.d.	n.d.	1.5 ± 0.5	80/20	423	1290	543
Ru1/CNTo	1.3	188	1.9	1.3 ± 0.4	35/65	378	2038	633
Ru1/CNTo973	–	–	2.8	1.7 ± 0.6	–	393/432	–	–
Ru1/CNTo1173	–	–	3.6	1.8 ± 0.5	–	432	1118	412
Ru2/CNTp	–	–	6.5	4.0 ± 1.3	90/10	–	1384	295
Ru2/CNTo	2.7	186	6.4	3.8 ± 1.1	40/60	381	2618	799
Ru2/CNTo973	–	–	7.9	3.9 ± 1.3	–	–	1236	752
Ru2/CNTo1173	–	–	10.4	6.1 ± 2.4	–	–	–	–

<sup>a</sup> From XRD.

<sup>b</sup> From TEM.

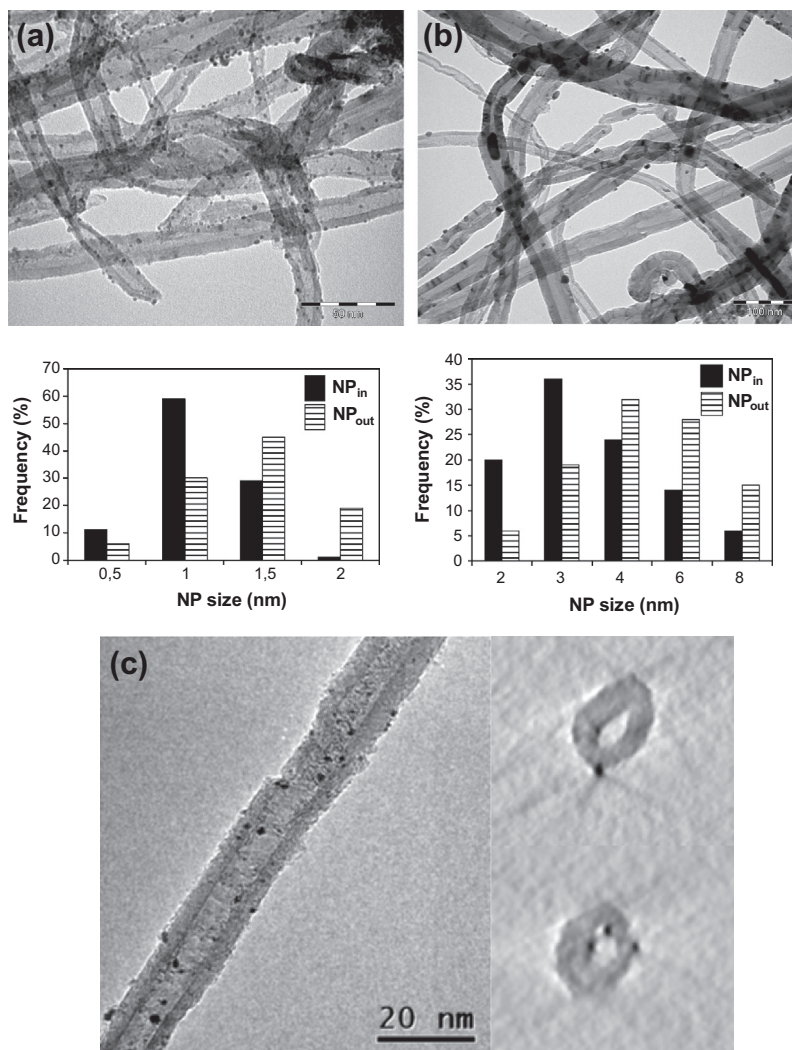


**Fig. 3.** Representative TEM micrographs and particle size distribution of (a) Ru1/CNTo (scale bar = 50 nm), (b) Ru2/CNTo (scale bar = 100 nm), and (c) Left: TEM image extracted from the tilt series used to reconstruct the volume of the analyzed Ru1/CNTo fragment. Right: two typical transversal slices from the calculated reconstruction.

particle sizes), supports the fact that these new groups are associated with ruthenium. It is worth noting that the generally accepted processes for the production of ruthenium acetate involve reacting Ru salts with either acetic acid or acetic anhydride. Additionally, ruthenium is known to be an active catalyst for ring-opening polymerization of lactones [43]. At this stage, two hypotheses can be formulated. Either the reaction of the ruthenium precursor with the carboxylic, anhydride, and lactone groups created a more stable kind of CO<sub>2</sub> releasing species, the stability of which could depend among others on nanoparticle size, or the reaction of the ruthenium precursor with these groups creates acetato grafted molecular Ru species, which may decompose, catalytically or not, at a temperature close to the one of the original oxygen SFG. In that case, the reduction at 573 K should contribute to the decomposition of those former groups, and then, a surface reconstruction should occur, creating more stable groups. Concerning the first hypothesis, TPD experiments were performed (see SI.4) on the impregnated catalyst prepared from **Ru1** (**Ru1\*** sample, dried at 353 K and unreduced). The TPD-MS profiles of Ru1\*/CNTo showed that most of the anhydride and lactone groups have disappeared and that CO<sub>2</sub> is evolved at a temperature very close to that observed for the **CNTo** sample (560 K for **CNTo** and 575 K for Ru1\*/CNTo). If Ru-surface acetato ligands species are formed, their stability is similar to that of the –COOH SFGs. Hence, the first hypothesis can be rejected.

TPD-MS profiles of Ru<sub>x</sub>/CNTo1173 sample show that, even if on those sample, most of the oxygen SFGs have been removed by the heat treatment, a surface reconstruction reaction is still occurring. In that case, this reaction produces groups that evolve CO<sub>2</sub> upon decomposition but in lower amounts and at higher temperatures. This phenomenon might also be correlated to ruthenium NPs size. Although a linear correlation between the temperature of decomposition of these groups and the mean Ru particle diameter was not obtained (see SI.5), a tendency is clearly observed. It was also checked by performing two consecutive TPD experiments (without air re-exposure) on Ru1/CNTo samples that all the oxygen SFGs were effectively removed.

As far as the CO evolution profile is concerned, an increase in the intensity of the peak at 870–880 K was noticed, attributed to epoxy groups, upon Ru deposition. Interestingly, epoxy groups are still present on the samples heat treated at 1173 K, suggesting their reformation during the surface reconstruction reaction. The formation of epoxy groups for the Ru1/CNTp sample was also noticed (SI.6), for which the Ru loading is very low.

The part of CNT spontaneous re-oxidation in air after a heat treatment of the **CNTo** sample at 1173 K was evaluated separately (see SI.7). Since TPD is performed under helium, the removal of oxygen SFGs should create a relatively reactive surface. Even if it has been proposed that nitrogen heat-treated carbon samples (to remove the oxygen SFGs) can quickly re-adsorb oxygen at ambient

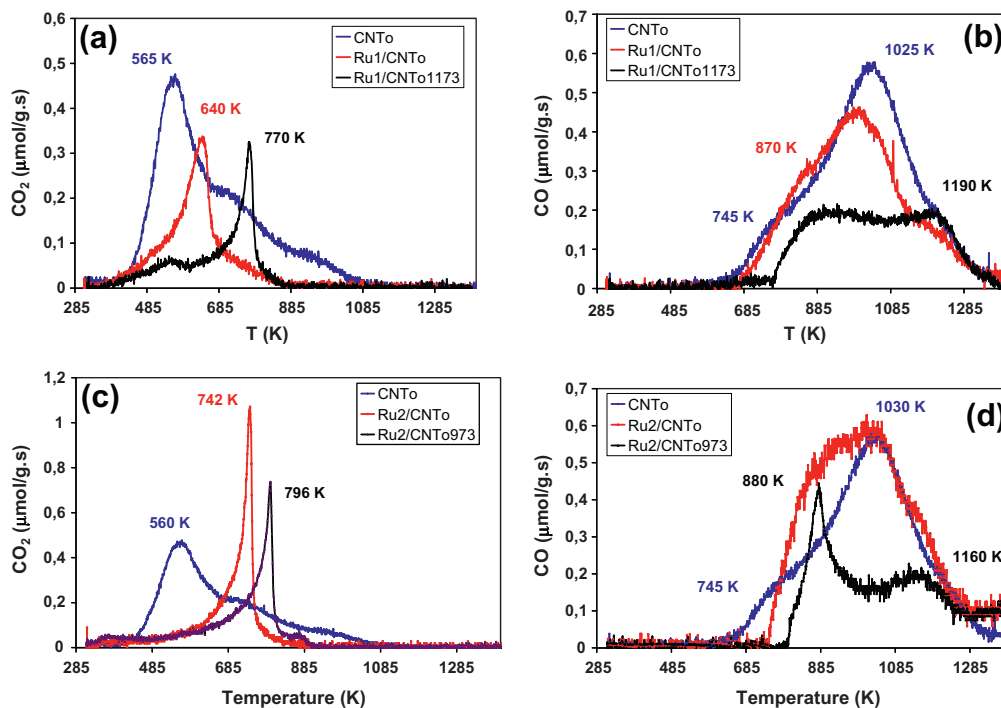


Fig. 4. TPD-MS profiles of the carbon-supported ruthenium samples, (a) and (c)  $\text{CO}_2$  evolution, and (b) and (d) CO evolution.

conditions due to the creation of active sites at the edges [44], in the case of CNTs, this re-oxidation is negligible. Indeed, the amount of CO and  $\text{CO}_2$  evolved before and after the heat treatment at 1173 K under  $\text{N}_2$  were 2248  $\mu\text{mol/g}$  (CO, CNTo), 606  $\mu\text{mol/g}$  (CO, CNTo1173), 1244  $\mu\text{mol/g}$  ( $\text{CO}_2$ , CNTo), and 126  $\mu\text{mol/g}$  ( $\text{CO}_2$ , CNTo1173). All these data suggest that the surface reconstruction should involve the following: (i) the ruthenium NPs, (ii) surface carbon atoms, and (iii) a source of oxygen. The mechanism of this reaction has been investigated by DFT (see Section 3.3). Concerning the source of oxygen, it can be either (i) oxygen SFGs that have not been decomposed, (ii) new oxygen SFGs that could have formed upon air exposure of the reduced catalysts, or (iii) oxygen arising from a thin  $\text{RuO}_x$  layer that can form upon air exposure of the reduced NPs. This surface reconstruction reaction, which leads to the formation of an Ru-acetato interface, and of epoxy SFGs occurs either at room temperature, during the air exposure of the reduced samples, or during the TPD experiment under He.

**3.1.2.3. TPR analyses and catalyst stability.** The TPR profiles of Ru1/CNTo and Ru2/CNTo are relatively similar and show a narrow  $\text{H}_2$  consumption peak centered at 380 K, and a very broad peak at around 750 K (see Fig. 5).

Similar profiles, but temperature-shifted, were obtained for Ru/CNT catalysts prepared from  $\text{RuCl}_3$  [15]. Two minor peaks were observed, for Ru1/CNTo at 555 K and for Ru2/CNTo at 445 K. Three types of reducible ruthenium species can be envisaged: (i) Ru species anchored on the external CNT walls via surface acetato ligands, (ii) Ru species anchored on the external CNT walls via a perfect or defective (vacancies) graphene surface, and (iii) Ru species anchored on the internal CNT walls via a perfect or defective (vacancies) graphene surface. It results from literature analysis that ruthenium is reduced at a lower temperature ( $345 \text{ K} < T < 428 \text{ K}$  for  $\text{RuCl}_3$  or  $\text{Ru}(\text{NO})(\text{NO}_3)_3$  precursors) [44–46] on oxidized CNTs, than on pristine CNTs ( $440 \text{ K} < T < 450 \text{ K}$  for the  $\text{Ru}(\text{NO})(\text{NO}_3)_3$  precursor) [47,48]. It has also been shown that NPs located inside CNTs can be reduced at a lower temperature than NPs deposited on the external surface [49]. The first intense peak at 380 K and

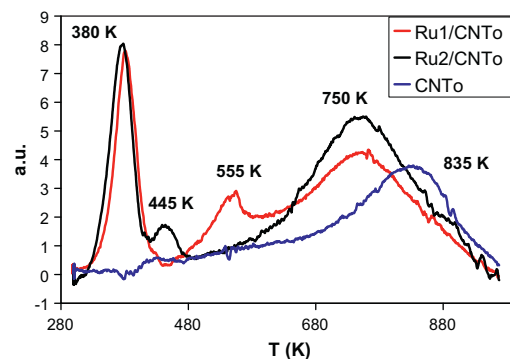


Fig. 5. TPR profiles of the carbon-supported ruthenium samples.

the low intensity peak at 445 K (Ru2/CNTo) have been attributed to the reduction of ruthenium present in two different environments. Since Ru2 is less reactive than Ru1 toward oxygen SFGs (see Section 3.2), it is proposed that the low intensity peak at 445 K is associated with the reduction of Ru bound to external surface sites that do not contain oxygen (possibly vacancies), while the intense peak at 380 K is associated with the reduction of ruthenium particles grafted to the external oxygen SFG or to the internal surface.

Hydrogen consumption on Ru/C catalysts can be associated with three distinct phenomena: (i) ruthenium oxide reduction, (ii) reaction with carbon due to surface oxygenated functional groups removal, and (iii) methanation. It has been reported that, at around 773 K, the reaction of hydrogen on noble metal-supported carbon material can generate basic carbon surfaces thanks to hydrogen spillover [50]. The role of the noble metal is to produce atomic hydrogen, which spills over onto the carbon surface and hydrogasifies the most reactive unsaturated carbon atoms, at lower temperature than molecular hydrogen. As far as the large peak centered at around 750 K is concerned, it is generally assigned to metal-assisted hydrogasification of surface carbon atoms in the

vicinity of metal particles and/or to reaction of H<sub>2</sub> (or H atoms resulting from spillover) with reactive carbon sites formed upon oxygen SFG removal, producing C–H bonds [44]. The shifting of the position of this peak from 835 K for the pristine CNTo support to 750 K for the Ru supported samples confirms that ruthenium should be involved in this process.

TPR profiles were also recorded for the Ru1 series (SI.8). The effect of heat treatment on TPR profiles can be summarized as follows: (i) the ruthenium reduction peak shifts to higher temperature (380 K → 425 K) anticipating a different metal–support interaction, which was confirmed by the TPD data, where we observed a shift of the CO<sub>2</sub> sharp peak upon heat treatment, and (ii) a significant decrease in the intensity of the high-temperature hydrogen consumption peak. The decrease in intensity of this latter peak indicates that the associated H<sub>2</sub> consumption is mainly correlated to the concentration of oxygen SFGs. Thus, we believe that in the case of CNT support, the hydrogasification reaction that produced methane should be very limited. Instead, in the presence of ruthenium, atomic hydrogen, which spills over onto the CNT surface, is produced and then reacts with the active carbon atoms formed upon oxygen SFG removal to produce C–H bonds, and eventually one molecule of methane [51]. It is worth mentioning that H<sub>2</sub> can also assist the removal of oxygen SFGs [52,53]. Previous comparisons of TPR and TPD for thermal desorption of CO, CO<sub>2</sub>, and water-vapor have shown that (i) hydrogen may facilitate the desorption of carboxylic anhydride, (ii) some CO surface groups, probably semi-quinone, can be directly reduced by hydrogen to form water, and (iii) a net hydrogen evolution from the carbon surface starts at temperatures above 1150 K [52,53].

The limited hydrogasification and CH<sub>4</sub> formation should result from the orientation of the graphene layers in CNTs that differ from that observed on conventional carbon supports such as activated carbon, carbon black, highly oriented pyrolytic graphite, few-layer graphene, or diamond crystallite, for which the concentration of edges is much higher. These latter carbon materials can be catalytically etched by hydrogen gas at high-temperature assisted by various metal nanoparticles as catalysts [54,55]. This reaction, which usually produces nano-holes or nano-channels, can be used, for example, to increase the density of mesopores into activated carbon [56], or for nanopatterning of graphene [57,58]. To check that the catalytic etching producing methane *via* hydrogasification was more pronounced on carbon support presenting a high edge/basal plane ratio, we studied the reaction of H<sub>2</sub> at 973 K for 1 h with three different materials: Ru/CNTo, Ru/CNFo, and Ru/FLGo (where CNFo consists in HNO<sub>3</sub> oxidized herringbone carbon nanofibers, and FLGo HNO<sub>3</sub> oxidized few-layer graphene). Fig. 6 shows TEM micrographs taken before and after the reactions. The TEM micrographs clearly show that on supports presenting a high edge/basal plane ratio (CNFo and FLGo) the catalytic etching is much more pronounced, creating holes (Ru/CNFo) or channels (Ru/FLGo), and inducing a severe sintering of ruthenium nanoparticles. These experiments point out the high stability of the Ru/CNTo catalyst. Catalytic etching and severe sintering (mean particle size 6.1 nm) was only observed for the Ru/CNTo sample after reaction in Ar/H<sub>2</sub> at 1173 K (see SI.9).

The catalyst characterization provides two important pieces of information, concerning the nature of the metal–support interaction. First, Ru1 reacts with anhydride, lactone and carboxylic groups to form a species grafted to the surface, probably through an acetato surface ligand. Upon reduction at 573 K, the acetato surface ligand decomposes and Ru nanoparticles are produced. Upon air exposure, the ruthenium surface is oxidized and a surface reconstruction reaction occurs that involves Ru, oxygen (probably from RuO<sub>x</sub>), and reactive surface carbon atoms to produce a new acetato surface ligand for the nanoparticles, and epoxy SFGs. Second, the fact that CNTs present a low edge/basal plane ratio

contributes to catalyst stability. In the following sections, additional experiments as well as DFT calculations were performed in order to get further information on the following: (i) the ruthenium precursor and NP anchoring (Section 3.2) and (ii) the mechanism of the surface reconstruction reaction (Section 3.3).

### 3.2. Experimental and theoretical studies on ruthenium anchoring

#### 3.2.1. Reactivity of the Ru precursors with anthracene derivatives

In order to better understand the anchoring mechanism of the ruthenium precursor on the CNT surface, the reactivity of Ru1 and Ru2 toward anthracene and several oxygenated anthracene derivatives as analogues to the CNT surface was investigated. In a screw cap NMR tube, the ruthenium precursor was dissolved in acetone-d<sub>6</sub> and an excess of anthracene (2 eq.) was added to the yellow solution. After heating at 318 K overnight, the <sup>1</sup>H NMR spectrum was recorded at room temperature. As expected, the ruthenium complexes did not react with the aromatic rings. It has been demonstrated that no ligand displacement on [Ru(COD)(COT)] complex by aromatic hydrocarbons takes place in the absence of molecular hydrogen [59]. As CNTs contain several oxygenated SFGs, we performed the same experiment with several oxygenated anthracene derivatives (9-anthracenecarboxylic acid, 9-anthracenecarboxaldehyde, and 9-anthracenol, Scheme 2). None of these species react with [Ru<sub>3</sub>(CO)<sub>12</sub>]. The aldehyde and the alcohol derivatives did not react with [Ru(COD)(COT)], even after long periods of reaction (until 60 h at 318 K). On the other hand, the carboxylic acid derivative induced the formation of a yellow precipitate in the NMR tube after heating 20 h at 318 K. The <sup>1</sup>H NMR spectrum recorded *in situ* showed that the supernatant contains 1,3-cyclooctadiene, traces of 1,5-cyclooctadiene and unreacted 9-anthracenecarboxylic acid. The NMR tube solution was evaporated to dryness and the yellow solid was re-dissolved on CD<sub>2</sub>Cl<sub>2</sub> and a second <sup>1</sup>H NMR spectrum was recorded. The <sup>1</sup>H NMR spectrum showed the formation of a new ruthenium complex. The reaction was scaled-up in order to obtain [Ru(9-anthracenecarboxylate)<sub>2</sub>(COD)] as a yellow solid in moderate yield (63%, see experimental section). Single crystals of [Ru(η<sup>2</sup>-9-anthracenecarboxylate)<sub>2</sub>(COD)] suitable for X-ray diffraction were obtained by slow diffusion of pentane into a solution of the complex in dichloroethane (see SI.10). The structure confirmed the formation of the neutral ruthenium complex.

#### 3.2.2. DFT study on the adsorption mode of Ru nanoparticles on the carbon support

The possible anchoring modes of Ru nanoparticles on CNT side-walls were investigated by DFT calculations, by using a simple model made of a Ru<sub>13</sub> cluster and a graphene monolayer (ML). Table 3 summarizes the main geometrical and energetics aspects of the adsorption of the Ru<sub>13</sub> cluster on a pristine graphene ML (Gr-Pr), as well as in the vicinity of a stable di-vacancy defect (Gr-DV). Since after HNO<sub>3</sub> treatment –COOH groups are present, we also performed calculations with a graphene ML presenting one or two –COOH groups, named Gr-Carb1 and Gr-Carb2, respectively, and a ML presenting a di-vacancy, decorated by one or two carboxylic groups (Gr-DV-Carb1, Gr-DV-Carb2). The mono-vacancy case was excluded from our study, since after HNO<sub>3</sub> treatment such highly reactive sites will be passivated due to –COOH groups formation, as recently reported [39].

Without any surface oxidation of the perfect graphene ML, the NP's adsorption induces distortions of the NP itself and a small corrugation of the support appears, with positive and negative changes in height of 0.16 Å (see Fig. SI.13). The corresponding adsorption energy is –234 kJ/mol, a result in good agreement with a recent theoretical work [31]. Considering the nanocluster geometry, the free standing I<sub>h</sub>-Ru<sub>13</sub> has Ru–Ru distances from the

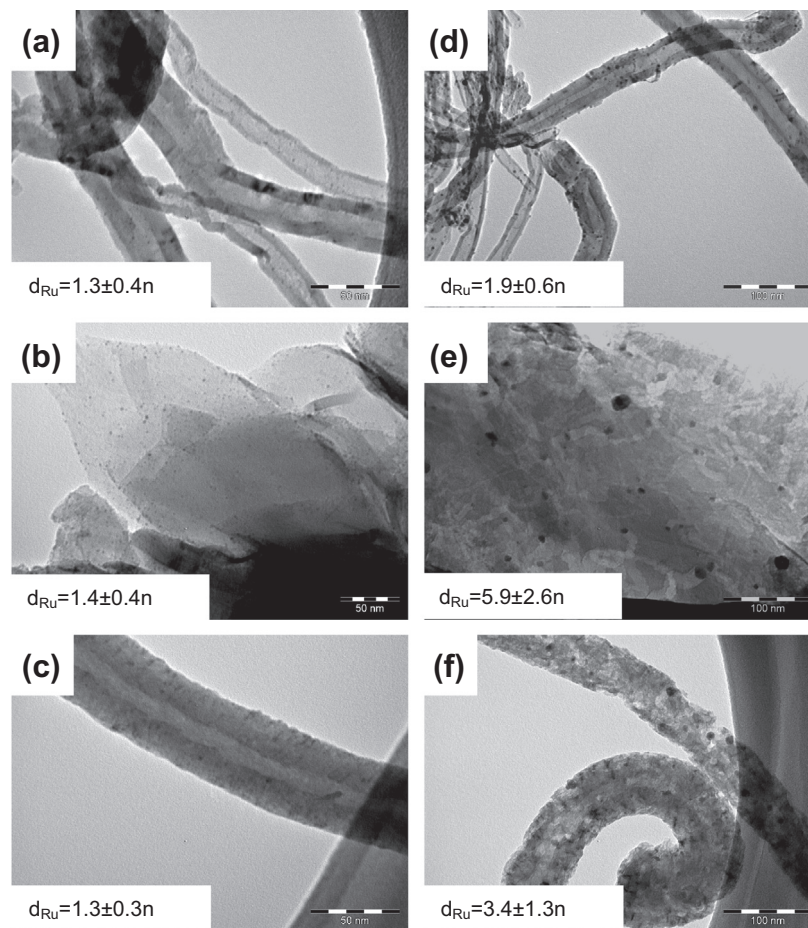
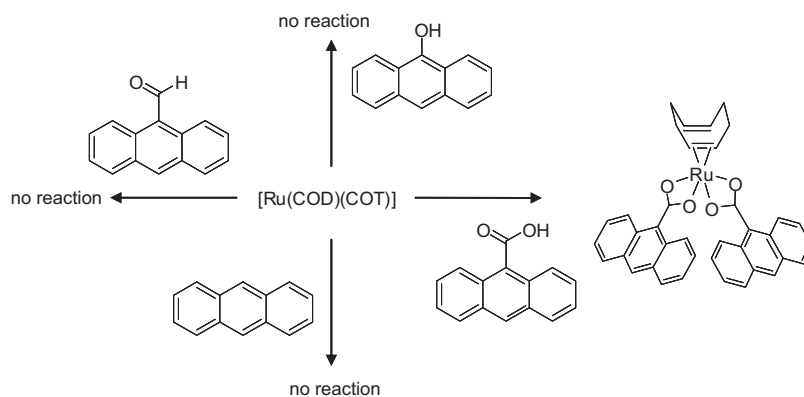


**Fig. 6.** TEM micrographs of (a, d) Ru/CNTo, (b, e) Ru/FLGo, and (c, f) Ru/CNFo before (a, b, and c), and after (d, e, and f) reaction with an Ar/H<sub>2</sub> mixture at 973 K.



**Scheme 2.** Reactivity of [Ru(COD)(COT)] toward anthracene derivatives.

**Table 3**

Characteristic parameters of the adsorption mode of an icosahedral Ru<sub>13</sub> nanocluster on a pristine or functionalized graphene monolayer.

	Gr-Pr	Gr-DV	Gr-Carb1	Gr-Carb2	Gr-DV-Carb1	Gr-DV-Carb2
<i>E</i> <sub>ads</sub> (in kJ/mol)	−234	−406	−264	−151	−226	−448
Adsorption modes	4-coord	3-coord	5-coord	2-coord	2-coord	5-coord

central atom, ranging between 2.50 and 2.53 Å with its 12 neighbors. Upon adsorption, its symmetry is lost; the central atom is now bound to 10 atoms in the first sphere of coordination with interatomic distances varying from 2.46 to 2.60 Å, while the two remaining atoms are now 3.44 Å away. The nanocluster is

tetra-coordinated to the support. A first Ru atom is bound to 3 C atoms with a mean bond-length of 2.24 Å, while the average over the 6 Ru–C distances is around 2.29 Å for the second Ru atom. Additionally, the two other Ru atoms are in bridge position with average bond-lengths of 2.35 Å. A structural defect (Gr-DV) binds

more strongly the nanocluster, with a binding energy of 406 kJ/mol, without any drastic geometrical modifications. The coordination mode implies 3 Ru atoms, two in a  $\mu^3$  position and one in a  $\mu^5$  as shown in Fig. SI.14.

After nitric acid treatment, the presence of carboxylic groups at the CNT surface clearly influences the adsorption modes of the NPs. For instance, the interaction of the Ru<sub>13</sub> nanocluster on top of a single-COOH group (Gr-Carb1 model) is less strong (−71 kJ/mol) than with the pristine surface and leaves the Ru<sub>13</sub> particle symmetric (see SI.15). When a second −COOH group interacts with the aggregate (Gr-Carb2 case), the binding energy becomes 151 kJ/mol. This stable state results from the formation of two Ru–O bonds of 2.10 and 2.13 Å, when the smallest Ru–H distance is 2.25 Å. A stronger binding can be obtained since the Ru<sub>13</sub> aggregate binds laterally to a −COOH group, as shown in SI.15. The Ru<sub>13</sub> cluster keeps its strong interactions with honeycomb's C atoms, and at the same time, allows the interactions between 3 Ru atoms and the SFGs group, one interacting with the C atom, with a Ru–C distance of 2.08 Å, the other two being in interaction with the two O atoms. The corresponding Ru–O distances are 2.11 and 2.23 Å. The energy stabilization, estimated to be −264 kJ/mol, is larger than the pure case. The presence of surfacic carboxylic groups favors the anchorage of NPs, thanks to an additional lateral interaction.

The situation is even more favorable as soon as structural defects are involved. As it is shown in Table 3, on a DV decorated by a carboxylic group, the binding is already competing with the adsorption mode on the pristine surface. The spontaneous proton's jump to the Ru<sub>13</sub>'s closest edge added to the formation of two Ru–O bonds of 2.09 and 2.04 Å explains the energy's stabilization (geometry is provided in SI.16). The hydride nature of the adsorbed H has been confirmed by charge analysis. The carboxylate group of Gr-DV-Carb1 is then stable, contrarily to the non-defective surface, since all our attempts to transfer one or two protons from Gr-Carb1 or Gr-Carb2 models to the Ru<sub>13</sub> particle have released a CO<sub>2</sub> molecule. The most stable adsorption mode appears to be the Ru<sub>13</sub> in interaction with the DV decorated by 2 carboxylic groups, with a complex grafting mode as shown in Fig. 7.

Three Ru atoms are bound to the graphenic substrate: one is  $\mu^3$  with Ru–C distances of 2.22, 2.23 and 2.32 Å, one is laying 2.32 Å above a C atom, while the third is in bridge position with a distance of 2.11 and 2.15 Å. It also interacts with the C atom of the closest un-dissociated carboxylic group, with a Ru–C distance of 2.15 Å. Moreover, one Ru atom interacts with the same group through a Ru–O distance of 2.00 Å, while another Ru atom interacts with the other −COOH group with Ru–C and Ru–O distances of 2.04 and 2.15 Å, respectively. Again, the main part of the interaction is due to strong Ru–C interactions, slightly reinforced by some Ru–O interactions. Unlike the Gr-DV-Carb1 case, no spontaneous proton transfer occurs. By overcoming an energy barrier of 75 kJ/mol, which corresponds to the O–H bond breaking, the adsorption energy is additionally lowered by 54 kJ/mol. Thus, the hydride stands in a  $\mu^3$  position, while an additional Ru–O bond of length 2.03 Å is formed (Fig. 7, right).

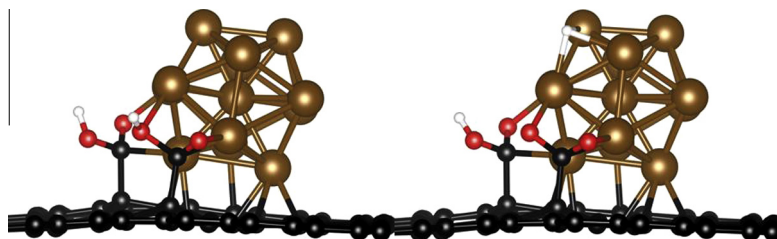


Fig. 7. Side-views of Ru<sub>13</sub> adsorbed on Gr-DV-Carb2 before (on left panel) and after a proton jump (right panel). C atoms are in black, O in red, H in white and Ru in mocha. (For interpretation of the references to colour in this figure legend, the reader is referred to the web version of this article.)

In conclusion, the interaction between Ru NPs and the pure support is already strong. Indeed, if one considers the ideal situation with the Ru<sub>13</sub> aggregate in interaction with a pure graphene substrate, the binding energy per contact Ru atom is 59 kJ/mol. This value has to be compared to 6 kJ/mol per contact Ru atom, extracted from a recent calculation [60], dealing with the interaction between a corrugated graphene ML and Ru (0001) surface. In our approach with a small (0.5 nm) cluster model, the C–Ru interaction is overestimated. It is due to the presence of very reactive edges and apexes on small aggregates, not present on larger NPs, which exhibit flat, more compact and so less reactive surfaces. Secondly, the presence of very stable structural defects like DV stabilizes the NP anchorage. Moreover, the presence of additional carboxylic groups, which may transfer protons spontaneously or with a low activation barrier, is also a stabilizing agent. From our coordination mode forecasts, one could expect that these SFGs would be more present at the NP's periphery than at the Ru–C interface. To our opinion, the results extracted from our models, considering the energetic aspects mainly, can be viewed as upper limits of larger NPs grafting modes.

### 3.3. Surface reconstruction reaction upon re-oxidation due to air exposure

Re-oxidation process has been investigated, assuming that after heat treatment, most of the oxygenated SFGs have been removed from the carbon honeycomb structure. We have also assumed that the oxygen source, involved in the formation of epoxy and carboxylate, is O<sub>2</sub> molecules. From ultra-high vacuum experiments, oxygen molecules spontaneously dissociate on close packed Ru (0001) surfaces [61]. It is also the case when an O<sub>2</sub> molecule approaches an edge of the Ru<sub>13</sub>, with an energy drop of 293 kJ/mol per atomic O. It results in two O in top position, with a Ru–O distance of 1.70 Å. These surfacic O atoms are relatively mobile since the energy barrier for the hopping process is 54 kJ/mol. This value can be viewed as an upper limit of the barrier of surfacic diffusion process of O atoms on larger NPs, since on Ru (0001) surface, it has been theoretically estimated to be 48 kJ/mol [62]. This small difference originates from the higher plasticity of the small nanocluster, compared to a rigid Ru (0001) surface.

Due to the presence in excess of O<sub>2</sub>, we further hypothesize that small NPs will be completely oxidized; while large ones will probably be coated by a thin RuO<sub>x</sub> film. This has been verified by a series of calculations, where we have checked that a freestanding Ru<sub>13</sub> NP can easily absorb up to 30 O atoms, a number slightly in excess in comparison with the standard stoichiometric RuO<sub>2</sub> case. It is a thermodynamically favorable configuration since the adsorption energy per O atom is still −167 kJ/mol. After oxidation, the I<sub>h</sub> structure is preserved, and the O atoms occupy bridge positions with all the Ru–O distances being 1.97 Å; see top panel of Fig. 8.

When this oxidized nanocluster interacts with Gr-Pr or Gr-DV, it undergoes strong distortions upon relaxation, as it is shown in Fig. 8. In the Gr-Pr case, the oxidized aggregate spreads out,

enhancing the contact area, with a maximal extension of more than 12 Å. On the 555-777 defect, the nanocluster remains more compact, no longer than 10 Å. The oxidized aggregate is only weakly bound to the pure graphene ML, with large O–C distances around 3.7 Å, the minimal distance being 3.19 Å. The corresponding adsorption energy is –84 kJ/mol. The Ru<sub>13</sub>O<sub>30</sub> system also interacts weakly with the 555-777 defect, with an adsorption energy of –67 kJ/mol. In both cases, the formation of the Ru-oxide strongly weakens the interaction with the carbon-based substrate.

Assuming that the source of the new oxygen SFGs is atomic O present at the RuO<sub>x</sub>-graphene interface, we have investigated possible pathways of O-release on the graphene layer, mainly by hopping processes, involving one or two O atoms from the oxidized nanocluster to the graphene ML with and without defect. Considering that the process is thermodynamically driven, if one assumes that it happens at room temperature, it means that the final state, *i.e.* oxygen atoms chemically bound to one or more C atoms of the support and possibly to Ru atoms too, has to be lower in energy than the initial state, with the concerned O atom in interaction with Ru atoms.

Transferring one O atom from the Ru<sub>13</sub>O<sub>30</sub> on Gr-Pr or on Gr-DV is thermodynamically unfavorable, since the corresponding energy differences are largely positive, as reported in Table 4. In such a configuration, no spontaneous jump of an atomic O will occur from the oxidized nanocluster to the graphene ML. We have checked that the removed O atom from the aggregate adopts the most stable configuration on a graphene ML, *i.e.* in bridge position, to form an epoxy group, as reported in the literature [63]. For sake of comparison, the energy difference corresponding to the reaction involving Pr-Gr and ½ O<sub>2</sub> to form an epoxy group is also positive and is around 46 kJ/mol. Neither the spontaneous dissociation of O<sub>2</sub>, nor the transfer of one atomic O from a saturated Ru-oxide thin film is responsible for the reformation of epoxy or carboxylate groups. An excess of O atoms at the interface between the oxidized nanocluster and the graphenic substrate is mandatory.

By adding an extra O at the interface (see the top panel of Fig. 9 for the pristine case), the nanocluster structure is weakly changed. This extra atom weakens slightly the interaction between the oxidized aggregate and the substrate, since the adsorption energies increased only by +13 kJ/mol in the Gr-Pr case. The same value is obtained in the Gr-DV case. From this stable configuration, there is a strong tendency of an atomic O transfer from the oxidized nanocluster to the pure graphene ML. Indeed, a significant energy difference is yielded (–96 kJ/mol) as soon as the

**Table 4**

Energy differences (in kJ/mol) between several initial and final states for one atomic O jump from the oxidized nanocluster to the carbonaceous substrate.

	Ru <sub>13</sub> O <sub>30</sub>	Ru <sub>13</sub> O <sub>30</sub> + 1 O	Ru <sub>13</sub> O <sub>30</sub> + 2 O
Gr-Pr	+138	–96	+50
Gr-DV	+117	+38	–25

interfacial O atom binds to the honeycomb structure to form an epoxy group with a C–O distance of 1.46 Å. The closest atom of the nanocluster becomes the oxygen attached to the graphene ML at the distance of 3.16 Å. To reach this state, an energy barrier of 117 kJ/mol has to be overcome, a value compatible with experimental observations. Fig. 9 provides also transition state and final geometries of this single atomic O jump. The late transition states' geometry is mainly characterized by an O–O bond of 1.56 Å and a C–O bond of 1.60 Å.

On top of the 555-777 defect, the most stable configuration of this extra O atom is when it lies over a C–C bond shared by a pentagon and a hexagon, with  $d_{C-O} = 3.09$  Å. However, the atomic O jump is not thermodynamically allowed, since the energy difference is *ca.* +38 kJ/mol. It is only when a second extra O lies below the oxidized surface too that makes the transfer possible. Keeping the first O atom at the same position, the second atomic O is just over the opposite C–C bond, shared with a 7-ring ( $d_{C-O} = 2.88$  Å). If this atom jumps to the graphenic substrate to form an epoxy group shared by the closest 5 and 7 carbon cycles, with a C–O distance of 1.45 Å, the energy difference becomes slightly negative. If one allows the second extra O to adsorb to the graphene ML, the energy difference is positive again (+29 kJ/mol). This indicates that there is a need of extras O atoms at the interface, less bound to the oxidized NP, to be more easily transferred to the carbon network. In other words, to allow for oxygen transfer, the NP surface has to be saturated to coordinate as much as possible interfacial ruthenium atoms. This saturation is certainly possible upon air exposure due to the excess of O<sub>2</sub> molecules that can easily dissociate, associated with the good mobility of atomic O on the Ru NP surface. Interestingly, the carbon atoms involved in 5 or 7-rings appear to be not much different than 6-ring C atoms to accept O atoms, since they do not facilitate the oxygen transfer.

Finally, when the Ru<sub>13</sub>O<sub>32</sub> nanocluster interacts with the pristine surface, the energy difference corresponding to a single jump is positive again (+50 kJ/mol), but the corresponding final

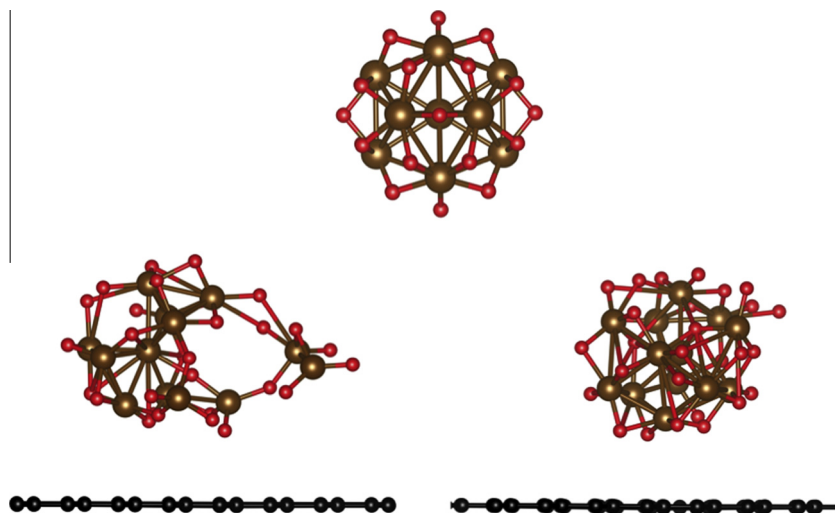


**Fig. 8.** Geometries for Ru<sub>13</sub>O<sub>30</sub> before (top panel) and after adsorption on Gr-Pr (left bottom panel) and Gr-DV (right bottom panel). C atoms are in black, O in red, H in white and Ru in mocha. (For interpretation of the references to color in this figure legend, the reader is referred to the web version of this article.)

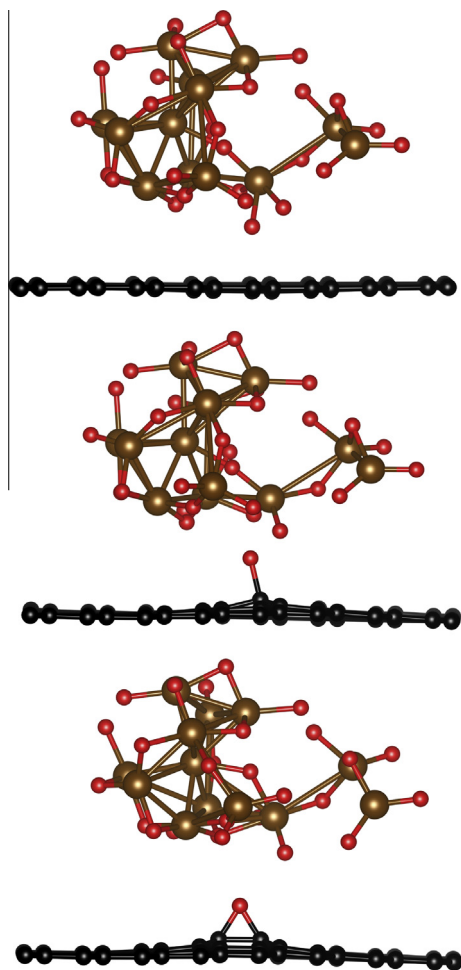


**Fig. 9.** Geometries of  $\text{Ru}_{13}\text{O}_{30} + 1 \text{ O}$  atom on Gr-Pr. Top panel shows the initial state, in the middle lies the transition state geometry while the bottom panel shows the final state with the epoxy group. C atoms are in black, O in red, H in with white and Ru in mocha. (For interpretation of the references to color in this figure legend, the reader is referred to the web version of this article.)

geometry presents an interesting feature. The interfacial O atom forms a bond with the above Ru atom (1.97 Å) and at the same time pulling out a carbon atom of the substrate, as shown in Fig. 10 (top panel). The C–O distance is 1.50 Å when the elevation of the carbon atom out of the plan is around 0.6 Å. Assuming that a second O jumps in the vicinity of this anchorage point, or if one O atom could arrive in this area due to hopping process on the graphene surface, all the conditions to form a carboxylate group bound to a Ru atom of the nanoparticle are met (middle panel of Fig. 10). Indeed, we have calculated that the energy barrier for a single O atom to jump from a bridge position to the closest one is only 71 kJ/mol, meaning that epoxy groups are mobile on the CNT sidewalls, under experimental conditions.

Starting from the structure depicted in the mid-panel of Fig. 10, the presence of the Ru atom over the C–C bond and the relatively small Ru–O distance 2.46 Å will certainly facilitate the hopping of the second oxygen in order to form a stable carboxylate group (bottom panel of Fig. 10). These 3 configurations are relatively close together in energy. The first structure is more stable by over 113 kJ/mol than the second one. But if one considers that each time an oxygen atom leaves the aggregate another one takes its place, the system will gain around 137 kJ/mol at most per each replacement, the presence of the epoxy group in the vicinity of the Ru–O–C bridge is thermodynamically allowed. Moreover, the relatively modest model of NP we used is certainly too malleable in

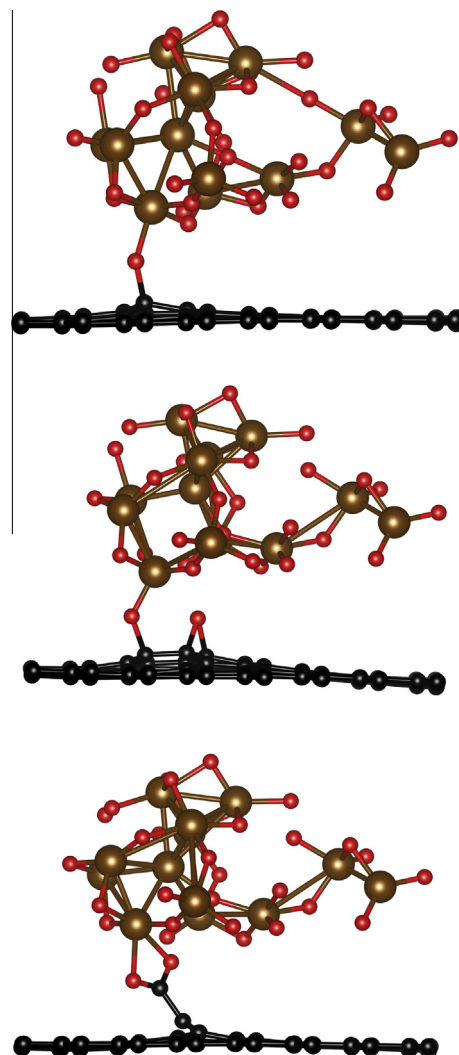


**Fig. 10.** Geometries of  $\text{Ru}_{13}\text{O}_{30} + 2 \text{ O}$  atom on Gr-Pr after one O transferred to the ML (top) and the final geometry after the second atomic O jump (middle panel). The last panel shows a possible structure presenting a stable carboxylate group at the interface. C atoms are in black, O in red, H in with white and Ru in mocha. (For interpretation of the references to color in this figure legend, the reader is referred to the web version of this article.)

comparison with larger systems. As a consequence, strong atomic reorganization of the nanoparticle is possible that increases energy differences. Indeed, the carboxylate group, despite its interaction with the interfacial Ru atom, is around 126 kJ/mol higher than the previous state, but with some structural changes in the oxidized NP. Some Ru–O bonds are elongated by few tenths of angstroms.

From these theoretical data, it means that in this scenario of sidewall's re-oxidation, there is a need of atomic O accumulation at the oxidized Ru-surface-CNT sidewall interface, to favor the atomic O transfer to the support. These transfers have low energy barriers and are thermodynamically driven. Additionally, in the case of a pristine substrate, we have provided theoretical evidences that the formation of a carboxylate group is even possible at the interface. It appears that this interfacial functional group is more stable than a surfacic carboxylate group, in good agreement with experiments. Indeed, due to their deep location at the interface, the interfacial carboxylates have a shorter C–C bond 1.48 Å compared to 1.58–1.63 Å, and which we obtained in the case of SFGs. A possible reason for this stronger binding is the more  $sp^2$

pronounced character of the basal C that allows for a larger delocalization of charge coming from the two O atoms.

#### 4. Conclusions

The complex surface chemistry of carbon materials, which is confirmed in this work, often induces the use of empiric approaches for metal-supported catalyst preparation. In the present experimental and theoretical study, CNTs have been used as a model support of the carbon surface. The role of oxygen SFGs on ruthenium grafting has been elucidated and is limited to exohedral functionalization. The ruthenium(0) precursor [Ru(COD)(COT)] anchors on the external surface of oxidized CNTs by acetato ligands *via* a reaction with carboxylic, carboxylic anhydride, and lactone groups. Endohedral Ru grafting should occur preferentially on DV, which provide good stabilization of Ru NPs. The reduced particles located inside CNTs, CNT<sub>in</sub> (~60% of the NPs) present a smaller diameter than the CNT<sub>out</sub>, whatever the Ru precursor used. The DFT calculations showed that the Ru<sub>13</sub> cluster binds stronger to a graphene double vacancy than to the pristine graphene. The adsorption energy of the icosahedral Ru<sub>13</sub> cluster followed the trend: Ru/Gr-DV-(COOH)<sub>2</sub> > Ru/Gr-DV > Ru/Gr. It has been evidenced that once exposed to air, the reduced Ru NPs are still anchored to the support *via* acetato ligands. Upon air exposure, the ruthenium surface is easily oxidized and a surface reconstruction reaction occurs involving Ru, oxygen (from RuO<sub>x</sub>), and reactive surface carbon atoms to produce a new acetato surface ligand for the nanoparticles, and epoxy SFGs. The same phenomenon occurs if, after a high-temperature treatment performed between 973 and 1173 K to remove the SFGs, the Ru NPs are re-exposed to air. This surface reconstruction can occur either on the perfect graphene surface or on defects, suggesting that it can also concern the Ru NPs located in the inner cavity. This surface reconstruction reaction can be seen as the first step toward RuO<sub>x</sub> reduction by the carbon support that will finally produce CO<sub>2</sub>. The thermal stability of the newly formed-COORu surface groups is higher than that of the initial-COOH groups. The Ru/CNT catalysts prepared are extremely stable, keeping high dispersion and small NP size even after heat treatment at high temperature. This remarkable stability can be attributed to the low edge/basal plane ratio present on the CNT support. This work sheds a new light on a general approach for designing highly stable carbon-supported nanocatalysts with desired structures for targeted reactions and could pave the way to the rational design of metal-carbon hybrid materials.

#### Acknowledgments

Prof. J.L. Faria and Mrs. R. Marques are acknowledged for their help in TPD analyses. The authors acknowledge financial support from the French CNRS (FR3507) and CEA METSA network. B.F.M. acknowledges Fundação para a Ciência e a Tecnologia for the grant SFRH/BPD/70299/2010. M.O. thanks the LIA Laboratoire de Chimie Moléculaire Maroco-Français, and the C'Nano GSO network for financial support. M.T. acknowledges the financial support from the European Project POCO, 7th Framework Program, Contract No. CP-IP 2139391. T.T.N.G. thanks the USTH consortium and the Ministry of Education and Training of Vietnam for her PhD grant. I.C. Gerber thanks the CALcul en Midi- Pyrénées (CALMIP, Grant 2012/2013-P0812) for generous allocations of computer time. This work was also performed using HPC resources from GENCI-TGCC and GENCI-CINES Grant 2013-096649.

#### Appendix A. Supplementary material

Supplementary data associated with this article can be found, in the online version, at <http://dx.doi.org/10.1016/j.jcat.2013.09.016>.

#### References

- [1] P. Serp, J.L. Figueiredo, Carbon Materials for Catalysis, John Wiley & Sons, Hoboken (NJ), 2009.
- [2] B.R. Cuenya, Thin Solid Films 518 (2010) 3127–3150.
- [3] C. Wen, Y. Liu, F. Tao, Pure Appl. Chem. 83 (2011) 243–252.
- [4] G.A. Somorjai, Y. Li, Proc. Natl. Acad. Sci. 108 (2011) 917–924.
- [5] J.K. Nørskov, F. Abild-Pedersen, F. Studt, T. Bligaard, Proc. Natl. Acad. Sci. 108 (2011) 937–943.
- [6] J.-M. Basset, R. Psaro, D. Roberto, R. Ugo, Modern Surface Organometallic Chemistry, Wiley-VCH Verlag GmbH & Co. KGaA, Weinheim, 2009.
- [7] T.J. Bandosz, Surface Chemistry of Carbon Materials, in: Carbon Materials for Catalysis, John Wiley & Sons, Inc., 2008, pp. 45–92.
- [8] C. Prado-Burguete, A. Linares-Solano, F. Rodríguez-Reinoso, C.S.-M. de Lecea, J. Catal. 115 (1989) 98–106.
- [9] F.J. Derbyshire, V.H.J. de Beer, G.M.K. Abotsi, A.W. Scaroni, J.M. Solar, D.J. Skrovaneck, Appl. Catal. 27 (1986) 117–131.
- [10] J.H. Bitter, K.P. de Jong, Preparation of Carbon-Supported Metal Catalysts, in: Carbon Materials for Catalysis, John Wiley & Sons, Inc., 2008, pp. 157–176.
- [11] J.L. Figueiredo, M.F.R. Pereira, M.M.A. Freitas, J.J.M. Órfão, Ind. Eng. Chem. Res. 46 (2006) 4110–4115.
- [12] A. Sepúlveda-Escribano, F. Coloma, F. Rodríguez-Reinoso, Appl. Catal. A 173 (1998) 247–257.
- [13] A. Guerrero-Ruiz, P. Badenes, I. Rodríguez-Ramos, Appl. Catal. A 173 (1998) 313–321.
- [14] P. Serp, M. Corrias, P. Kalck, Appl. Catal. A 253 (2003) 337–358.
- [15] J. Teddy, A. Falqui, A. Corrias, D. Carta, P. Lecante, I. Gerber, P. Serp, J. Catal. 278 (2011) 59–70.
- [16] M.L. Toebes, F.F. Prinsloo, J.H. Bitter, A.J. van Dillen, K.P. de Jong, J. Catal. 214 (2003) 78–87.
- [17] F. Coloma, A. Sepúlveda-Escribano, J.L.G. Fierro, F. Rodríguez-Reinoso, Appl. Catal. A 150 (1997) 165–183.
- [18] M.L. Toebes, Y. Zhang, J. Hájek, T. Alexander Nijhuis, J.H. Bitter, A. Jos van Dillen, D.Y. Murzin, D.C. Koningsberger, K.P. de Jong, J. Catal. 226 (2004) 215–225.
- [19] A. Altomare, G. Cascarano, C. Giacovazzo, A. Guagliardi, J. Appl. Crystallogr. 26 (1993) 343–350.
- [20] G.M. Sheldrick, Acta Crystallogr., Sect. A 64 (2008) 112–122.
- [21] O. Ersen, J. Werckmann, M. Houllé, M.-J. Ledoux, C. Pham-Huu, Nano Lett. 7 (2007) 1898–1907.
- [22] J.-P. Tessonnier, O. Ersen, G. Weinberg, C. Pham-Huu, D.S. Su, R. Schlögl, ACS Nano 3 (2009) 2081–2089.
- [23] G. Kresse, J. Furthmüller, Comput. Mater. Sci. 6 (1996) 15–50.
- [24] G. Kresse, J. Hafner, Phys. Rev. B 47 (1993) 558–561.
- [25] G. Kresse, J. Furthmüller, Phys. Rev. B 54 (1996) 11169–11186.
- [26] G. Kresse, J. Hafner, Phys. Rev. B 49 (1994) 14251–14269.
- [27] G. Kresse, D. Joubert, Phys. Rev. B 59 (1999) 1758–1775.
- [28] P.E. Blöchl, Phys. Rev. B 50 (1994) 17953–17979.
- [29] J.-P. Perdew, K. Burke, M. Ernzerhof, Phys. Rev. Lett. 77 (1996) 3865–3868.
- [30] G.-D. Lee, C.Z. Wang, E. Yoon, N.-M. Hwang, D.-Y. Kim, K.M. Ho, Phys. Rev. Lett. 95 (2005) 205501.
- [31] X. Liu, K.X. Yao, C. Meng, Y. Han, Dalton Trans. 41 (2012) 1289–1296.
- [32] I. Fampiou, A. Ramasubramaniam, J. Phys. Chem. C 116 (2012) 6543–6555.
- [33] G. Kim, S.-H. Jhi, ACS Nano 5 (2011) 805–810.
- [34] D.-H. Lim, J. Wilcox, J. Phys. Chem. C 115 (2011) 22742–22747.
- [35] P.E. Blöchl, O. Jepsen, O.K. Andersen, Phys. Rev. B 49 (1994) 16223–16233.
- [36] G. Henkelman, B.P. Uberuaga, H. Jonsson, J. Chem. Phys. 113 (2000) 9901–9904.
- [37] G. Henkelman, H. Jonsson, J. Chem. Phys. 113 (2000) 9978–9985.
- [38] K. Momma, F. Izumi, J. Appl. Crystallogr. 44 (2011) 1272–1276.
- [39] I. Gerber, M. Oubenal, R. Bacsa, J. Durand, A. Gonçalves, M.F.R. Pereira, F. Jolibois, L. Perrin, R. Poteau, P. Serp, Chem. Eur. J. 17 (2011) 11467–11477.
- [40] J.-H. Zhou, Z.-J. Sui, J. Zhu, P. Li, D. Chen, Y.-C. Dai, W.-K. Yuan, Carbon 45 (2007) 785–796.
- [41] H. Vu, F. Gonçalves, R. Philippe, E. Lamouroux, M. Corrias, Y. Kihn, D. Plee, P. Kalck, P. Serp, J. Catal. 240 (2006) 18–22.
- [42] A. Solhy, B.F. Machado, J. Beausoleil, Y. Kihn, F. Gonçalves, M.F.R. Pereira, J.J.M. Órfão, J.L. Figueiredo, J.L. Faria, P. Serp, Carbon 46 (2008) 1194–1207.
- [43] R.R. Gowda, D. Chakraborty, J. Mol. Catal. A: Chem. 301 (2009) 84–92.
- [44] J.A. Menéndez, L.R. Radovic, B. Xia, J. Phillips, J. Phys. Chem. 100 (1996) 17243–17248.
- [45] X. Yang, X. Wang, J. Qiu, Appl. Catal. A 382 (2010) 131–137.
- [46] T. Komanoya, H. Kobayashi, K. Hara, W.-J. Chun, A. Fukuoka, Appl. Catal. A 407 (2011) 188–194.
- [47] F.R. García-García, J. Álvarez-Rodríguez, I. Rodríguez-Ramos, A. Guerrero-Ruiz, Carbon 48 (2010) 267–276.
- [48] V. Jiménez, P. Panagiotopoulou, P. Sánchez, J.L. Valverde, A. Romero, Chem. Eng. J. 168 (2011) 947–954.
- [49] W. Chen, X. Pan, X. Bao, J. Am. Chem. Soc. 129 (2007) 7421–7426.
- [50] J. Xiong, X. Dong, L. Li, J. Nat. Gas Chem. 21 (2012) 445–451.
- [51] M. Cerro-Alarcón, A. Maroto-Valiente, I. Rodríguez-Ramos, A. Guerrero-Ruiz, Carbon 43 (2005) 2711–2722.
- [52] J.M. Calo, D. Cazorla-Amorós, A. Linares-Solano, M.C. Román-Martínez, C.S.-M. De Lecea, Carbon 35 (1997) 543–554.

- [53] B. Xiao, J.P. Boudou, K.M. Thomas, *Langmuir* 21 (2005) 3400–3409.
- [54] P.J. Goethel, R.T. Yang, *J. Catal.* 108 (1987) 356–363.
- [55] C.W. Keep, S. Terry, M. Wells, *J. Catal.* 66 (1980) 451–462.
- [56] T. Iwazaki, T. Semba, S. Konishi, T. Sezai, Y. Murakami, W. Sugimoto, Y. Takasu, *Chem. Lett.* 37 (2008) 1194–1195.
- [57] S.S. Datta, D.R. Strachan, S.M. Khamis, A.T.C. Johnson, *Nano Lett.* 8 (2008) 1912–1915.
- [58] L.C. Campos, V.R. Manfrinato, J.D. Sanchez-Yamagishi, J. Kong, P. Jarillo-Herrero, *Nano Lett.* 9 (2009) 2600–2604.
- [59] P. Pertici, G. Simonelli, G. Vitulli, G. Deganello, P. Sandrini, A. Mantovani, *J. Chem. Soc., Chem. Commun.* (1977) 132–133.
- [60] D. Stradi, S. Barja, C. Díaz, M. Garnica, B. Borca, J.J. Hinarejos, D. Sánchez-Portal, M. Alcamí, A. Arnau, A.L. Vázquez de Parga, R. Miranda, F. Martín, *Phys. Rev. Lett.* 106 (2011) 186102.
- [61] B. Herd, M. Knapp, H. Over, *J. Phys. Chem. C* 116 (2012) 24649–24660.
- [62] B. Hammer, *Surf. Sci.* 459 (2000) 323–348.
- [63] Ž. Šljivančanin, A.S. Milošević, Z.S. Popović, F.R. Vukajlović, *Carbon* 54 (2013) 482–488.